Phenomenology of Avalanche Recordings from Distributed Acoustic Sensing

Patrick Paitz[1], Nadja Lindner[2], Pascal Edme[2], Pierre Huguenin[3], Michael Hohl[3], Betty Sovilla[3], Fabian Walter[1], Andreas Fichtner[2]

[1]WSL, Swiss Federal Institute for Forest, Snow and Landscape Research, Birmensdorf, Switzerland
[2]ETH Zurich, Department of Earth Sciences, Institute of Geophysics, Seismology and Wave Physics
[3]SLF, WSL Institute for Snow and Avalanche Research SLF, Davos, Switzerland

Key Points:

- DAS measurements near the interface between avalanche and the subsurface reveal flow dynamics.
- Strain rate measurements of seismo-acoustic waves are registered up to 30 s before avalanches reach the sensors.
- Internal group velocities larger than the propagation speed suggest the presence of complex internal structures.

Corresponding author: Patrick Paitz, `patrick.paitz@wsl.ch`

Abstract

Avalanches and other hazardous mass movements pose a danger to the population and critical infrastructure in alpine areas. Hence, understanding and continuously monitoring mass movements is crucial to mitigate their risk. We propose to use Distributed Acoustic Sensing (DAS) to measure strain rate along a fiber-optic cable to characterize ground deformation induced by avalanches. We recorded 12 snow avalanches of various dimensions at the Vallée de la Sionne test site in Switzerland, utilizing existing fiber-optic infrastructure and a DAS interrogation unit during the winter 2020/2021. By training a Bayesian Gaussian Mixture Model, we automatically characterize and classify avalanche-induced ground deformations using physical properties extracted from the frequency-wavenumber and frequency-velocity domain of the DAS recordings. The resulting model can estimate the probability of avalanches in the DAS data and is able to differentiate between the avalanche-generated seismic near-field, the seismo-acoustic far-field and the mass movement propagating on top of the fiber. By analyzing the mass-movement propagation signals, we are able to identify group velocity packages within an avalanche that propagate faster than the phase velocity of the avalanche front, indicating complex internal structures. Importantly, we show that the seismo-acoustic far-field can be detected before the avalanche reaches the fiber-optic array, highlighting DAS as a potential research and early warning tool for hazardous mass movements.

Plain Language Summary

Avalanches and other hazardous mass movements pose a danger to the population and critical infrastructure in alpine areas. Therefore it is important to be able to reliably measure and detect these hazardous events. We show a successful example to measure and characterize avalanches recorded with a Distributed Acoustic Sensing (DAS) device, that measures deformation along a fiber optic cable. We apply unsupervised machine learning to our avalanche recordings, and are able to identify consistent properties between 12 avalanches. Ultimately, our results indicate that DAS might be a useful tool for detecting hazardous mass movements.

1 Introduction

1.1 Motivation

Practically all mountainous regions worldwide are subject to some forms of rock falls, snow/rock/ice avalanches, debris flows and sediment-transporting floods. These rapid mass movements pose a significant hazard to both the population and infrastructure, with billions of dollars in financial damage and thousands of fatalities each year (Emberson et al., 2020; Dilley, 2005; Froude & Petley, 2018; Petley, 2012). According to the 2021 Intergovernmental Panel on Climate Change (IPCC) report, the *"magnitude of debris flows might increase [...] and the debris-flow season may last longer in a warmer climate"* (Zhongming et al., 2021). This suggests that global warming will exacerbate the hazard potential of debris flows and various types of related mass movements. To early detect destructive events and mitigate their impact, extensive, reliable and high resolution monitoring and warning solutions are crucial. Seismic and acoustic instruments are increasingly popular for mass movement monitoring, since they record signatures of hazardous events even kilometers away from their occurrence without the need for a direct line of sight between source and sensor (Allstadt et al., 2018; Marchetti et al., 2019). The combination of unrivaled temporal resolution of seismic records and wide spatial sensitivity is a pivotal advantage over in situ measurements (Arattano & Marchi, 2008) and remote sensing approaches like radar technology (Leinss et al., 2020).

Implementation of seismic measurements into operational mass movement warning has to fulfill two requirements. First, the seismic sensors have to be placed in various locations to maximize coverage of failure-prone terrain. Second, the detection algorithms have to handle real-time data streams and reliably recognize significant telltale signals in the presence of environmental and anthropogenic noise.

Seismic instrumentation has in recent years undergone rapid developments towards more portable sensors (Leinss et al., 2020). However, even in densely instrumented countries like Switzerland, sensor coverage is still insufficient to encompass significant amounts of unstable slopes. In view of snow avalanches, in particular, the typically harsh terrain in avalanche-prone regions tends to limit the spatial coverage and temporal resolution of most measurements, and of seismic arrays in particular (Pérez- Guillén et al., 2016). Furthermore, recent improvements in machine learning algorithms show great promise for the automatic recognition of emergent and complicated mass movements seismograms (Chmiel et al., 2021). Yet further improvements are necessary to recognize events at sites where little or no training data are available and to identify signal characteristics, which reveal scientific insights into the dynamic characteristics of mass movements.

Here we address these open challenges with the applications of Distributed Acoustic Sensing (DAS) for snow avalanche detection and characterization. DAS is a technique to measure strain or strain rate along a fiber-optic cable with sub-meter resolution and mHz to kHz frequency bandwidth (Lindsey et al., 2020; Paitz et al., 2021). Unused fiber-optic infrastructure initially installed for communication purposes can thus be turned into countless seismic sensors increasing spatial coverage of seismic measurements. We leverage the dense seismic sensing of DAS with unsupervised algorithms to automatically recognize snow avalanches and their internal properties, offering new perspectives for monitoring and alarm systems.

1.2 Fiber-Optic Sensing in a Natural Hazard Context

The introduction of distributed fiber-optic sensing systems to geophysics marks a milestone. By turning a fiber-optic cable into a high resolution seismic measurement network, fiber-optic sensing technologies have opened up new possibilities in exploration geophysics and passive seismology (Lindsey & Martin, 2021; Zhan, 2019), especially in difficult terrain like glaciers and volcanoes (Klaasen et al., 2021; Walter et al., 2020) or on the bottom of the ocean (Lindsey et al., 2019; Williams et al., 2019). For more background information on fiber-optic sensing, the reader is referred to Hartog (2017).

In the context of natural hazards, Brillouin-based distributed fiber-optic sensing systems (BOTDA) have been utilized for landslide and deformation monitoring (Iten et al., 2008; Minardo et al., 2018), and coherent optical time-domain reflectometry (COTDR) was successfully used for ground motion and deformation measurements on landslides (Yu et al., 2018). The suitability of optical time-domain reflectometry (OTDR) systems like the Silixa iDAS(TM) Distributed Acoustic Sensing unit (used in this study) for the recording of acoustic emission precursors in soil in a laboratory setting was also already established several years ago (Michlmayr et al., 2017). The study by Walter et al. (2020) used a similar DAS system to successfully monitor rockfalls and icequakes on a glacier. Early studies by Prokop et al. (2014) explored avalanche monitoring with fiber-optic sensing systems for avalanche detection and runout distance monitoring.

2 Experiment Setup and Recorded Avalanches

We utilizied a Silixa iDAS(TM) v2.4 interrogation unit on an existing fiber-optic cable at the Vallée de la Sionne avalanche test site in Switzerland from October 2020 to March 2021. A map and a photograph of the test-site are shown in Fig. 1. The test site has been operated by the WSL Institute for Snow and Avalanche Research SLF for over 20 years (Ammann, 1999). Several sensor points within the avalanche paths and runout

zones feature seismic, pressure and radar sensors and are connected via fiber-optic cables to a bunker at the valley bottom where data are stored and processed. The length of the interrogated fiber was around 800 m, and the interrogator was located in the bunker, positioned at the bottom of the path. The fiber crosses the La Sionne creek around 700 m from the topmost monitoring point. Over the entire array, the (single-mode) fiber is installed in a conduit that was excavated to a depth of less than a meter during the construction of the test site. This protects the fiber against avalanche damages. The sampling rate of the interrogator was 1 kHz at a spatial sampling of 2 m.

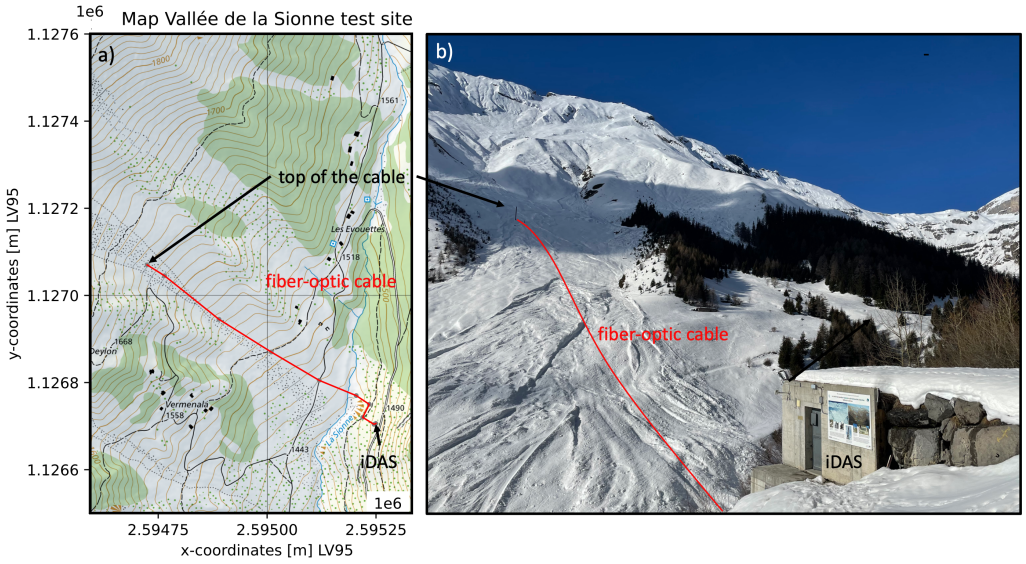

Figure 1. Test site overview. **a)** Map view of the Vallée de la Sionne avalanche test site. Map from SwissTopo (2021). **b)** Photograph of the test-site area with the approximate fiber position indicated in red. The DAS interrogation unit was located in the bunker (building in the lower right corner).

During the data acquisition period, more than 20 DAS recordings of avalanches were registered. In this manuscript, we first discuss the key characteristics for one example (denoted "avalanche 3023"). This one was selected since it contains key features while still being not too complex. For 12 additional events, the data are visualized in the supplementary material. The recorded data of the observed avalanches cover large transitional powder snow avalanches with partial flow regime transitions and depositional regimes (avalanches 3009, 3022 and 3023) and smaller avalanches without a clearly distinguishable transition (avalanches 3016, 3020 and 3021). A summary of the measured avalanches is given in Tab. B1 in the appendix.

3 Avalanche Recordings: Phenomenology

All avalanches considered in this study propagated on top of the fiber-optic cable. Therefore, the data contain a superposition of near-field observations of seismo-acoustic sources, as well as ground vibrations from sources that can potentially be further away. Note that we prefer the term "seismo-acoustic" over "seismic" as seismic records of avalanches may contain signatures of waves traveling through the air (Heck, Hobiger, et al., 2019). For particulate gravity currents like snow avalanches, various theoretical models for seismogenesis have been recently proposed, which form the basis for the following discus-

sion. Nevertheless, air waves such as infrasound may also contain important information about avalanche volumes and dynamics and could influence our DAS records (Allstadt et al., 2018; Marchetti et al., 2021).

For multiphase flows (granular flow in dense flow regimes and turbulent flow in the aerial components) such as snow avalanches, different seismic source mechanisms have been considered in the past: (1) (quasi-)static deformation as a response to instantaneous weight and frictional shear forces (Wenner et al., 2022) and (2) (snow) particle-ground impacts (Tsai et al., 2012), (3) turbulent flow (Gimbert et al., 2014) and, by (4) abrupt stopping of mass movement due to friction (Tregaskis et al., 2022), and by (5) changes in traction due to mass deposition and erosion (Edwards & Gray, 2015). A schematic avalanche propagating over our fiber array is shown in Fig. A1 in the appendix.

3.1 DAS data

3.1.1 Time-Distance Domain

The raw data of avalanche 3023 are visualized in Fig. 2. The total duration of the avalanche propagating over the array is about two minutes. The ground truth of the avalanche is confirmed by measurements of the GEODAR system (Keylock et al., 2014; Köhler, McElwaine, & Sovilla, 2018). The extent of the avalanche as measured by the GEODAR is highlighted in transparent blue colors in Fig. 2. Different parts of the avalanche can be distinguished (where the numbers correspond to the features highlighted in the figure): (1) The earlier, faster part of the avalanche between 0.5 and 1.0 minutes time, and (2) a slower, later part of the avalanche between 1.0 and 2.5 minutes. What is also visible is that (5) there are signals arriving over the entire array before the avalanche front moves on top of the cable (at times before 0.75 minutes). Other observable features include (4) noisier channels (e.g. at 310 meters), and (3) high amplitude and velocity events (nearly horizontal in the plot), spanning about 100 m in distance each. These events could be interpreted as (abrupt) stopping events, where parts of the avalanche abruptly decelerate, hence creating a high amplitude strain-change in the subsurface. Other potential explanations for these events include snowpack collapses. However the fact that the strain-rate amplitudes of the mass-movement is significantly lower after these events makes the abrupt stop hypothesis more likely. It must be noted that for distances above 200 m along the fiber, there is no clear DAS signal visible in the raw and low-frequency data, whereas the GEODAR outline still records an avalanche signal there. The low-frequency time-offset strain rate data are also visualized in Panel b) of Fig. 2. The two main parts of the avalanche (1) and (2), as well as the stopping mechanisms (3) are still visible, and the data look less noisy compared to the raw data in Fig. 2a).

3.1.2 Frequency-Wavenumber Domain

Since the fiber is approximately straight with equal channel spacing over the entire array, it is straightforward to analyze the data in the frequency-wavenumber domain. The frequency-wavenumber representation of the data is defined as a 2-D Fourier Transform (over time and over space):

$$\dot{\epsilon}(f,k) = \int_x \int_t \dot{\epsilon}(t,x)\, e^{-2\pi i f t}\, e^{-2\pi i k x}\, dt\, dx, \tag{1}$$

for the strain rate $\dot{\epsilon}$, time t, distance x, frequency f and wavenumber k (the inverse of the wavelength). This representation allows for analysis of the frequency and apparent phase velocity content of the data and can reveal dispersive behavior, i.e. frequency dependence of the velocity of individual wave modes.

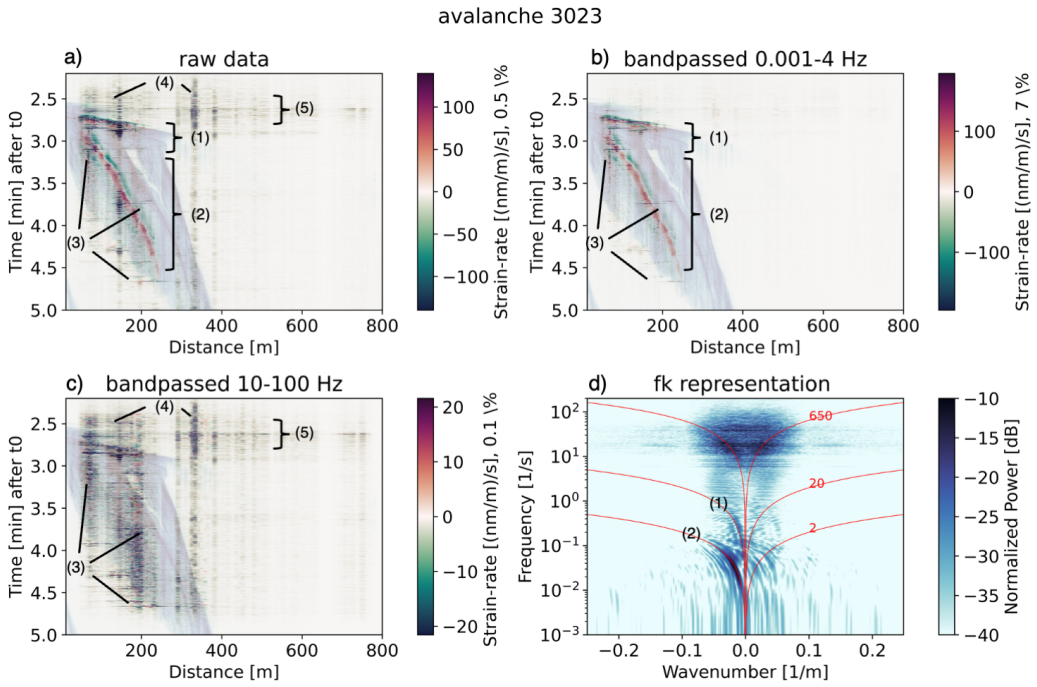

Figure 2. **a)** Raw strain rate data of avalanche 3023. The amplitudes are clipped at 0.5% of the global maximum within the visualized window. **b)** Bandpass filtered low-frequency strain rate data of avalanche 3023 (4th order Butterworth bandpass filter from 0.001 to 10 Hz). The amplitudes are clipped at 7 % of the global maximum within the visualized window. **c)** Bandpassed high-frequency strain rate data of avalanche 3023 (4th-order Butterworth bandpass filter from 10 to 100 Hz). The amplitudes are clipped at 0.1 % of the global maximum within the visualized window. For a) to c), the ground truth of the extent of the avalanche is highlighted in transparent blue from the measurements of the GEODAR system. **d)** Frequency-wavenumber (fk) representation of the raw data from avalanche 3023. The red lines indicate apparent phase velocities along the array in m/s. Negative wavenumbers indicate energy propagating from the top to the bottom of the slope (downward), and positive wavenumbers indicate coherent energy propagating upward. The distance starts at the Northwest end of the cable (uphill) at 0 m and ranges down to the Southeast end of the cable in the bunker, where the interrogator was located (Fig. 1).

The frequency-wavenumber (fk) representation of the raw data of avalanche 3023 is visualized in Fig. 2d. From the fk representation of the data, a clear separation can be observed between high-frequency seismic (10 - 30 Hz) and low-frequency (0.01 to 10 Hz) signals. The two different parts of the avalanche observed in the raw data are also visible in the fk domain (features (1) and (2)) for frequencies below 1 Hz. The fk visualization associates these low-frequency (< 1 Hz) downward propagating signals with phase velocities of between 5 to 20 m/s (1), and 2 m/s (2). In addition, high-velocity events are visible for frequencies between 5 and 30 Hz, propagating both up- and downward at speeds of about 650 m/s. Such apparent velocities and the omnidirectional propagation suggest that these events are seismic waves generated by the avalanche.

4 Signal classification

In order to automatically identify and distinguish between the signals shown in Fig. 2, we propose the use of unsupervised machine learning algorithms. In the past, unsupervised algorithms have proven useful in a geophysical context to extract subsets of signals with similar properties from large datasets (Martin et al., 2018; Grimm, 2021; Grimm & Poli, 2022). In a cryoseismic context, Grimm (2021) extracted different physical classes from continuous DAS recordings on a glacier, characterizing crevassing events, stick-slip icequakes and background noise in an automated way. Similarly, Grimm and Poli (2022) used spatial coherency features of an urban DAS dataset from Grenoble (France) to identify spatio-temporally repeating events. Martin et al. (2018) utilized signal features from data segments that had been transformed using the continuous wavelet transform and minibatch-optimized K-means to find classes of coherent properties of the seismic wavefield from DAS data. Here we propose to use unsupervised clustering to identify characteristic properties of avalanche recordings with DAS. Since the dimensionality of the DAS data is too high to perform clustering on raw data, we first extract representative features. This is a common first step in applied machine learning workflows, and the chosen features have to be chosen problem-dependent (Alpaydin, 2020).

4.1 Feature Extraction

Automatic and (near) real-time processing for warning applications requires signal feature extraction within small time- and space windows. These windows contain either avalanche signals and/or background noise, which includes natural (e.g., earthquake) and anthropogenic (e.g., road and air traffic) signals. We set the window sizes to 5 s in time and 50 m in space (with adjacent windows overlapping by 3 s and 30 m). The window size and overlap was chosen empirically such that coherent signals in time and space are detected, while small-scale changes are still captured.

Our proposed feature extraction algorithm is visualized in Fig. 3. In the first step, the raw data are windowed and transformed to the fk domain (see Eq. 3.1.2). In the fk domain, the contents of the amplitude spectrum of velocity-frequency bins are analyzed, resulting in cumulative fk amplitudes $\dot{A}$ for each bin, where the dot indicates that the cumulative fk amplitudes are associated with a transformation of strain rate $\dot{\epsilon}$ rather than strain.

$$\dot{A}(v_1, v_2, f_1, f_2) = \sum_{f,k} |\dot{\epsilon}(f,k)|; \;\; \forall\, v = \frac{f}{k} \in \{v_1, v_2\} \cap f \in \{f_1, f_2\}, \tag{2}$$

where the local phase velocity v can be described in terms of frequency f and wavenumber k, following $v = f/k$. The frequency and velocity bins range from f_1 to f_2 and from v_1 to v_2, respectively. The above equation maps our data from the fk domain into a discrete velocity-frequency (vf) domain. In the next step, we find n numbers of local maxima in this domain and extract the corresponding frequency and apparent velocity of these maxima, for both positive and negative wavenumbers. This results in n local maxima

for positive wavenumbers and negative wavenumbers:

$$M_n{}^{+}(v_{n^+}, f_{n^+}) = max(\dot{A}(v, f)); \ \forall n^+ \in \{1...n\} \cap k > 0 \tag{3}$$

$$M_n{}^{-}(v_{n^-}, f_{n^-}) = max(\dot{A}(v, f)); \ \forall n^- \in \{1...n\} \cap k < 0 \tag{4}$$

For each of these peaks $M_n(v_n, f_n)$, we compute the ratio $R(v_n, f_n)$ between the cumulative fk amplitudes $\dot{A}$ of positive and negative wavenumber, giving us an indication of a preferable directionality in propagation:

$$R_n{}^{+}(v_{n^+}, f_{n^+}) = \frac{\dot{A}(v_{n^+}, f_{n^+})}{\dot{A}(-v_{n^+}, f_{n^+})}; \ \forall n^+ \in \{1...n\} \cap k > 0 \tag{5}$$

$$R_n{}^{-}(v_{n^-}, f_{n^-}) = \frac{\dot{A}(-v_{n^-}, f_{n^-})}{\dot{A}(v_{n^-}, f_{n^-})}; \ \forall n^- \in \{1...n\} \cap k < 0 \tag{6}$$

In addition to the values of the peaks $M_n^{+|-}(v_n, f_n)$ in the vf domain, we extract information on the summed amplitude spectrum S, defined as:

$$S^+ = \sum_{f,k} |\dot{\epsilon}(f, k)|; \ \forall k > 0 \tag{7}$$

$$S^- = \sum_{f,k} |\dot{\epsilon}(f, k)|; \ \forall k < 0 \tag{8}$$

The last feature we extract is the ratio of cumulative amplitudes between positive and negative wavenumbers C within the specific time-space window:

$$C = \frac{S^+}{S^-}. \tag{9}$$

For each window, a total of 11 features are extracted per picked peak n as summarized in Tab. 1. This reduces the dimensionality for each window from 62500 (2500 samples for 25 channels) to $11{\cdot}n$, which is $< 0.1\%$ of the dimensionality of the raw data. In our case, n was chosen to be 3 in order to capture first, second and third order effects within each window. The features encode the apparent phase velocities, frequency content, dominant propagation direction and total strain rate energy within each window, and hence describe physical properties that are potentially important for avalanche characterization and discrimination from other signals like earthquakes.

4.2 Bayesian Gaussian mixture models: Unsupervised Clustering

The features in Tab. 1 are used in an unsupervised clustering algorithm to identify groups of data with similar properties. We chose a Bayesian Gaussian mixture model after evaluating the performance of various clustering algorithms including K-means, mini-batch K-means, and affinity propagation (Bishop & Nasrabadi, 2006; Press et al., 2007).

Bayesian Gaussian mixture models are probabilistic models that fit training data onto a finite number of Gaussian distributions, utilizing the Expectation-Maximization algorithm (see Bishop and Nasrabadi (2006); Press et al. (2007) for details). This way, each feature-set of the training data is associated to a cluster, or class (one of the Gaussian distributions). Compared to other conventional clustering algorithms like K-Means, Gaussian mixture models have the advantage that a trained model can predict a class from data that it was not trained with. Furthermore, instead of associating one class to a set of features (hard assignment of data points to a cluster), the probability of the data for being a part of each subclass is estimated (soft assignment of data points to a class from the posterior probabilities for each class) (Bishop & Nasrabadi, 2006), which in our

Table 1. Features extracted in each sub-window of the DAS record that are used for the characterization of the data.

Feature	Description
$M^+(v_{n^+}, f_{n^+})$	local maxima in the vf domain for positive k
$M^-(v_{n^-}, f_{n^-})$	local maxima in the vf domain for negative k
v_{n^+}, v_{n^-}	apparent phase velocity of the local maximum M for pos. (+) and neg. (-) k
f_{n^+}, f_{n^-}	frequency of the local maximum M for pos. (+) and neg. (-) k
$R^+(v_{n^+}, f_{n^+})$	ratio between $M^+(v_{n^+}, f_{n^+})$ and corresponding vf amplitudes of neg. k
$R^-(v_{n^-}, f_{n^-})$	ratio between $M^-(v_{n^-}, f_{n^-})$ and corresponding vf amplitudes of pos. k
S^+	cumulative amplitude spectrum in the fk domain for positive k
S^-	cumulative amplitude spectrum in the fk domain for negative k
C	ratio between S^+ and S^-

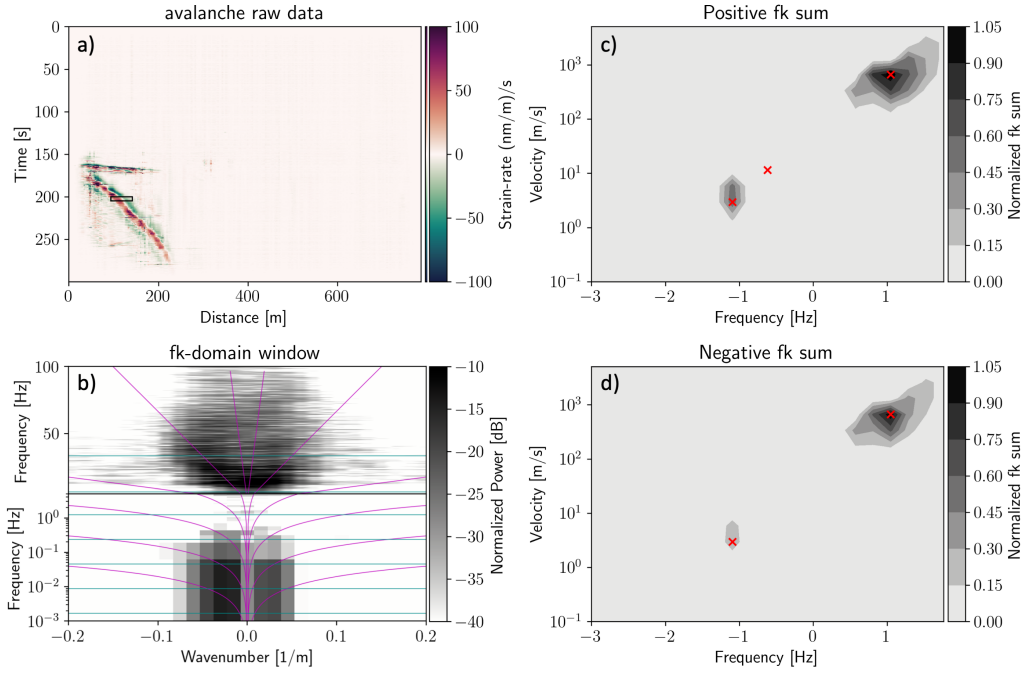

Figure 3. Example of the windowed algorithm proposed to extract signal properties used to detect and characterize avalanche data. **a)** In a first step, the data are windowed in both time and space (indicated by the black rectangle). In our example, the length of the window is 50 m and 5 s. **b)** The windowed data are then tapered (in both time and space) and transformed to the fk domain. The fk domain is then binned into frequency ranges (indicated by the horizontal blue lines) and velocity ranges (indicated by the magenta diagonal curves). For each bin, the absolute values of the fk amplitudes are then summed and normalized over the number of samples per bin. The fk domain amplitudes are displayed in dB relative to the maximum fk amplitudes. **c)** and **d)** The output of the bottom left is then arranged by frequency and velocity, and local maxima are extracted. This results in a number of n (in this example $n = 3$) extracted peaks, with corresponding frequency and velocity ranges, as well as summed fk amplitude values. The process is done for positive wavenumber values and for negative wavenumber values. For each peak, the ratio of positive to negative fk amplitude is also stored as a feature.

case becomes important where low-frequency low-velocity mass movements are within the same space time window as high-frequency seismic waves. We use the python package scikit-learn (Pedregosa et al., 2011) for the implementation of Bayesian Gaussian mixture models. Based on trial and error, we decided to set the number of classes to 10, initializing the weights, means and covariances with the K-means algorithm, and using a Dirichlet process for the weight concentration prior. Increasing the number of classes resulted in a higher number of "noise" classes without improving the signal classification. Decreasing the number of classes led to inconsistent clustering results for multiple stages of training.

We train the model with 92367 windows from 13 potential avalanche candidates, including windows containing environmental and anthropogenic noise, avalanches, and earthquake recordings. In total, 246118 feature sets are used as input for the training (where for some of the windows, less than 3 feature sets could be extracted). After training, the model can be used to estimate the probability of each class for all recorded time windows.

4.3 Clustering Results

The results of the Bayesian Gaussian mixture model analysis are visualized in Fig. 4 for avalanche 3023. They show the predicted classes with a probability higher than 0.3 for each window based on the trained model, together with a Gaussian kernel density estimation (Scott, 2015) for each class over both space and time. We can observe that both parts of the avalanche are classified within the same class S2 and that class S1 emerges 30 s before the avalanche propagates over the fiber-optic array. In addition, classes S3 and S4 are also associated with the avalanche, following the time after class S2 emerges. From the comparison of the kernel densities of the clustering result to the normalized cumulative GEODAR intensity, we can see a correlation of classes S2 to S4 with the ground truth of the GEODAR data.

5 Discussion: Physical Interpretation of the classes

Because the only available ground-truth data with spatial extent in the form of GEODAR data to highlight the physical extent of the avalanches, it is difficult to verify the hypotheses presented in this chapter. The provided physical interpretation given in this section should be seen as a highly speculative first attempt to illuminate the DAS avalanche recordings. Nevertheless, our interpretations are backed up by physical evidence from the properties of the different classes.

Since Bayesian Gaussian mixture models give us a probability distribution of any feature set being part of one specific class, we can predict the classes of our data to extract apparent phase velocity ranges, frequency content and dominant propagation direction of the measured signals. The clustering results for all investigated avalanches, as well as the mean feature values are visualized in Fig. 5. The results show consistency over all events and we show details of the space-time dependent classification of the DAS signals for Avalanche 3023 in Fig. 4.

Fig. 5 shows that whereas the classes denoted as noise N1 to N6 exhibit consistently low values in fk amplitudes (features M and S), they can be distinguished from each other in terms of apparent phase velocities and frequency ranges. Classes N1 and N2 consist of windows with dominant frequencies of ≤ 0.5 Hz. The noise classes N5 and N6 contain mainly frequencies above 5 Hz at apparent phase velocities higher than the ones from class N1 to N3 (> 350 m/s).

Class S3 is associated with the highest overall fk amplitudes at a mean frequency of around 16 Hz and a mean velocity of 1075 m/s, propagating both uphill and downhill along the cable (mean $C \approx 1.05$). This class can be interpreted as the **seismic near-**

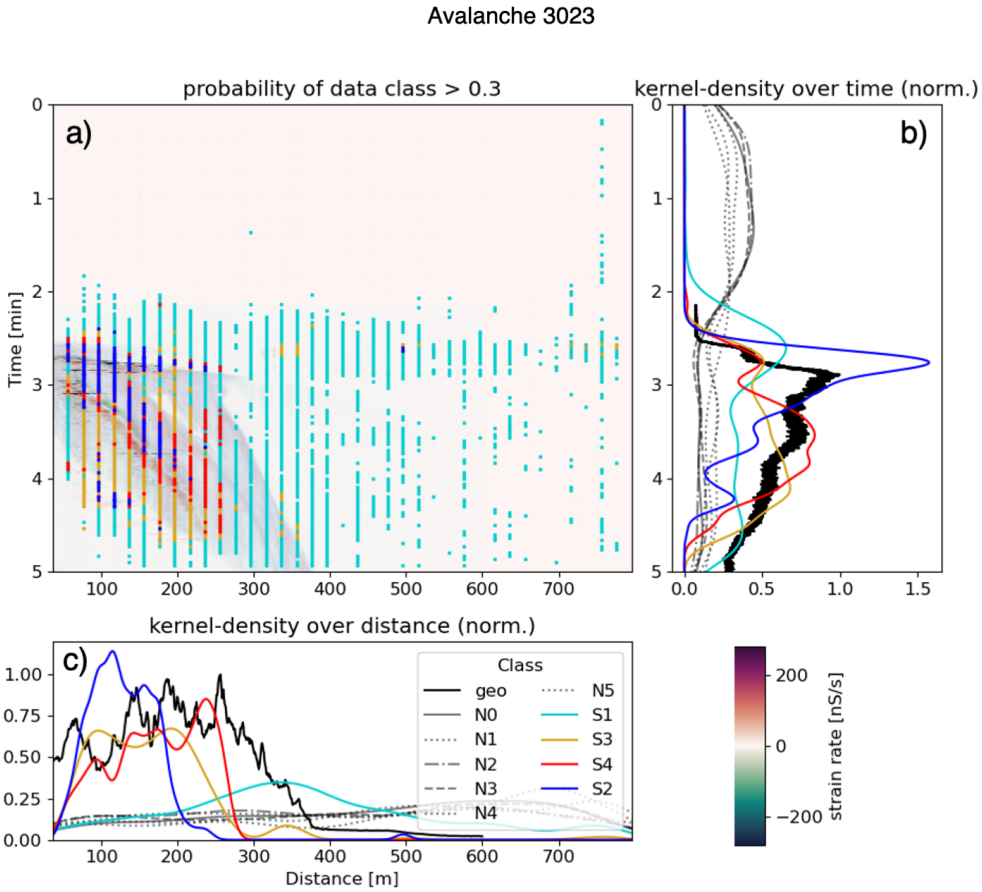

Figure 4. **a)** Results of the predicted classes with a probability above 0.3 for each window of the Bayesian Gaussian mixture model clustering for avalanche 3023. The raw strain-rate data are plotted in the background (see colorbar at the bottom right), whereas the predicted classes are color-coded for each class. The ground truth of the extent of the avalanche is highlighted in transparent blue from the measurements of the GEODAR system. Six different "noise" classes could be identified which are not visualized here (N1 to N6). These classes most likely capture environmental and anthropogenic noise, as well as self-noise of the instrumentation. **b)** Estimated probability density from a Gaussian kernel density over the samples within each class over time. The black line indicates the normalized cumulative GEODAR amplitudes for the given window. **c)** Estimated probability density from a Gaussian kernel over the samples within each class over space. The black line indicates the normalized cumulative GEODAR amplitudes for the given window

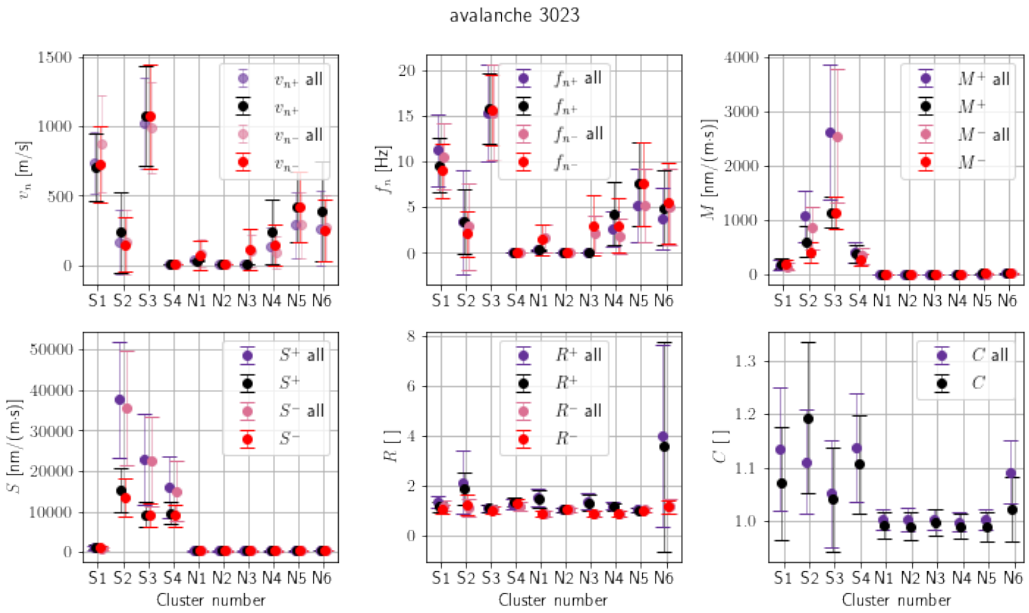

Figure 5. Mean feature values (dots) and $\frac{1}{2}$ standard deviation (error bars) for each clustered feature set of avalanche 3023. Black color indicates positive wavenumber-values (downward propagating energy, superscript $^+$) and red indicates negative wavenumbers (upward propagating energy, superscript $^-$) along the fiber for avalanche 3023. The purple and light red colors indicate the features for all the training data that were used in the clustering process.

field, as this class is dominant on channels during the time the avalanche is on top of the cable. These values are realistic for seismic waves in sediment layers (Boore & Joyner, 1997), especially considering that near-field signals consist of multiple seismic phases including P-waves. These are faster than Rayleigh phases, which are the dominant far-field response to vertical particle-ground impacts (Sánchez-Sesma et al., 2011).

Class S2 has a significantly lower mean frequency (3.4 Hz) and apparent velocity (238 m/s). This class has the highest mean C value (1.2), meaning that the dominant propagation direction of these signals is downhill. The apparent velocities are exceptionally low but could be explained by slow Biot's waves propagating through the pore space of snow within the avalanche and/or the underlying substrate (Capelli et al., 2016).

Based on the apparent velocity content (mean 703 m/s) of class S1, we interpret it as the **seismo-acoustic far-field** generated by the avalanches. This apparent velocity is reasonable for surface and S-waves in generic rock sites (Boore & Joyner, 1997). The frequency content (mean 9.6 Hz) of this class is comparable to the frequency range of seismic waves generated by avalanches observed in the literature (Van Herwijnen & Schweizer, 2011). The probability of class S1 increases already 30 s before the avalanche arrives at the cable. With the above mean frequency, mean velocity and typical avalanche speeds of several meters per second, this likely corresponds to a time when the avalanche is several wavelengths away from the cable, which supports our hypothesis of seismic far-field waves.

Class S4 contains frequencies below 1 Hz, which we interpret as quasi-static ground deformation in response to the instantaneous avalanche weight and frictional shear forces. Waves of such quasi-static ground deformation can result from flow depth, velocity or particle concentration perturbations traveling within the avalanche body (Viroulet et al.,

2018) and erosion-deposition mechanisms (Edwards & Gray, 2015). This explains the apparent phase velocities (< 6 m/s), associated with avalanche motion rather than seismic energy propagation of classes S1-S3. The motion of the avalanche front and major secondary surges induce wavelets with periods of ten seconds or longer (Fig. 2b, for example), which are not resolvable with our 5 second time window sizes. Nevertheless, class S4 seems to capture the highest frequencies of these signals. C values of larger than 1.1 indicate that S4 signals propagate preferentially downhill. Uphill propagation, however, is also possible and can be explained by shock wave dispersion (Liu & Mei, 1994).

So far we have discussed the avalanche signal in terms of dominant classes. However, this binary (dominant/non-dominant) characterization is not always justified since several classes may reach similar probabilities at the same location in space and time. This is particularly apparent for Avalanche 3016, whose DAS signals and kernel densities have a simple appearance since the avalanche consists of only one surge (Fig. 6). During times when Avalanche 3016 covers the cable, further signal details are visible and might be interpreted as the avalanche front (1), internal roll waves (2) or erosion-deposition waves (3) and stopping phases (4)(Razis et al., 2014; Viroulet et al., 2018; Tregaskis et al., 2022), travelling at different and variable speeds (different event move-outs in Fig. 6). In addition to class S4, classes S2 and S3 can also be expected to characterize these internal dynamic processes within the avalanche as like class S4 they dominate during times when the avalanche locates above the cable. In fact, for Avalanche 3016, kernel densities of classes S2, S3 and S4 increase and decrease parallel to each other and have comparable peaks (Fig. 6 panel b)).

From this figure we can also observe that the avalanche front propagates at a relatively high apparent group velocity of about 40 m/s (labeled (1)). Internal apparent phase velocities of up to 160 m/s are present in the earlier part of the avalanche (2). We can also observe the transition from class S2 towards S4 (panel b). This may be related to the transition from the erosive and intermittent flow-regime characteristic of the avalanche front towards the depositional flow regime at the avalanche tail (3) after around 3 min. The internal velocities of up to 160 m/s within the avalanche that are higher than the front propagation speed of around 40 m/s suggest that internal phases may be processes related to roll-waves activity taking place at the surface of the denser basal layer (Razis et al., 2014; Viroulet et al., 2018).

The above discussion shows that although different classes can be associated with characteristic ranges of frequencies and propagation velocities, they combine to describe avalanche dynamics. The arrival of the front with its instantaneous increase in local weight will induce low-frequency, quasi-static elastic deformation (class S4). This adds to weight variations resulting from snow entrainment, which for powder snow avalanches can take the form of violent eruptions (Carroll et al., 2012; Sovilla et al., 2006) and other internal phases or flow-depth variations like roll waves (Razis et al., 2014; Viroulet et al., 2018) to produce further low-frequency signals. At the avalanche front, we also expect the turbulent and suspended mass movement to couple into the ground (classes 1 and 3). Although we are not aware of theoretical descriptions of the seismogenesis of turbulent and laminar air-snow mixtures, an equivalent mechanism has been proposed for river flow (Gimbert et al., 2014). This leads to a mixing of signals from classes 1, 3 and 4. Similarly, temperature-dependent sintering produces macroscopic granules (Steinkogler et al., 2015) whose ground impacts generate high-frequency seismic signals (Tsai et al., 2012) constituting classes 1 and 3. It is not clear if these mechanisms also generate the slow seismic phases of class 2, which is a predominant signal when all avalanches override the cable. The existence of a potential Biot phase (Capelli et al., 2016) is possible but not the only explanation. The records of the local M 1.2 earthquake from Sanetschpass about 10 km from our recording site testify to the non-uniqueness of physical class meaning (see event 3036 in the supplementary material, occurring on March 03, 2021, 00:38:14 UTC): The DAS earthquake records lack class S4, which is expected as the earthquake

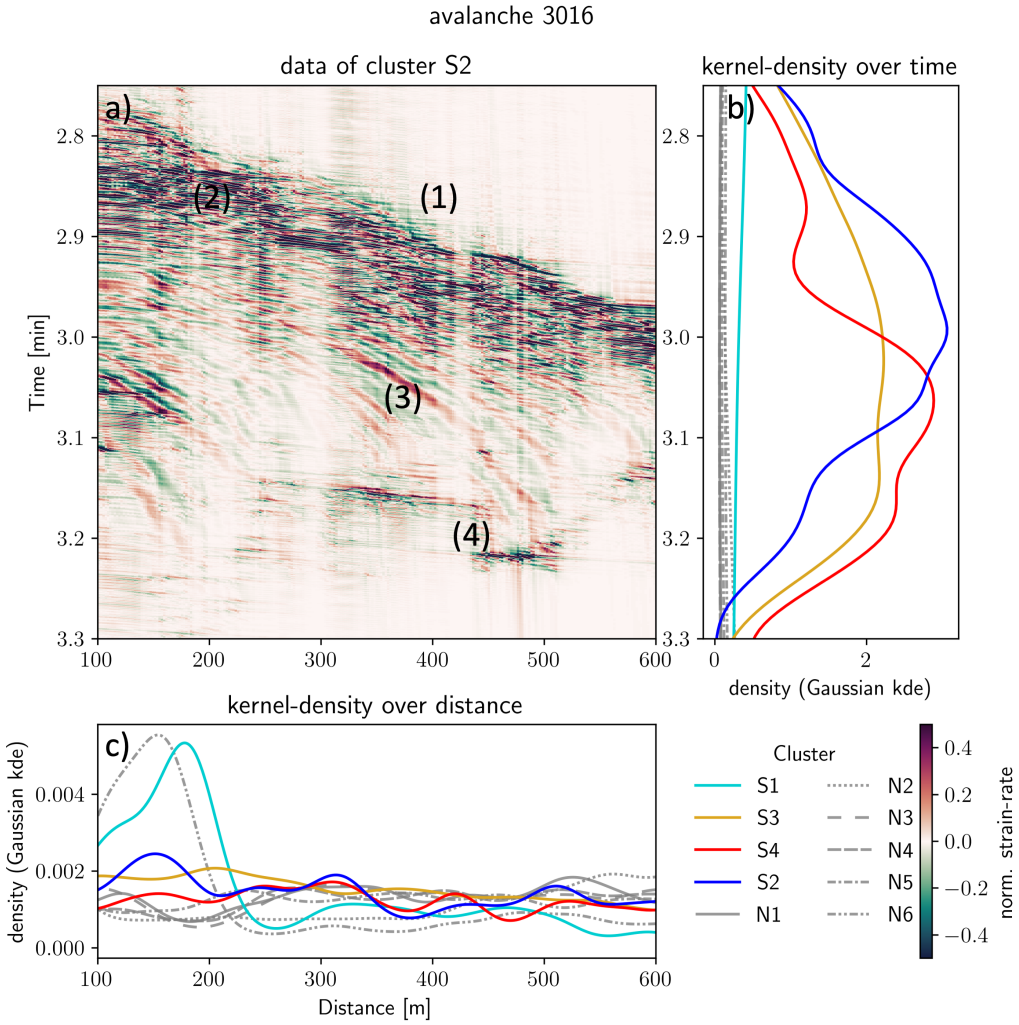

Figure 6. **a)** DAS data of avalanche 3016 in the frequency range from 0.001 to 5 Hz for apparent velocities between 1 and 250 m/s (corresponding to the mass-movement class S2). We can observe that the internal structure of the avalanche is more complex than for avalanche 3023. The group velocity of the avalanche front (1) is approximately 40 m/s, whereas the phase velocity inside the avalanche (2) is around 160 m/s. The later part of the avalanche lacks these high-velocity arrivals, and instead consists of events that decrease from 40 m/s until they stop (3). In the deposit area, other events (4) also seem to propagate at apparent phase velocities of $>$ 160 m/s downhill. **b)** Estimated probability density from a Gaussian kernel density over the samples within each class over time. **c)** Estimated probability density from a Gaussian kernel over the samples within each class over space.

does not generate slowly propagating signals corresponding to the quasi-static elastic ground deformation induced by an avalanche. On the other hand, the earthquake records are predominantly classified into classes S1 and S3. Our interpretation of S3 as near-field seismic signals at frequencies resolvable within 5 second time windows is questionable since the earthquake located 10 km away from the cable. The absence of class S2 suggests that this class is indeed characteristic for mass movements, even though an explanation of its rather slow seismic propagation speeds remains elusive.

To summarize, there exist distinct signal classes, which are shared among all of the recorded avalanches (classes S1 to S4). Class S1 is interpreted as the seismo-acoustic far-field that arrives at the cable before the mass movement itself. Classes S2-S4 are associated with low-frequency, quasi-static ground deformation, near-field ground shaking and other yet-to-be-confirmed signals generated as the avalanches override the cable. Although these interpretations may differ for other seismic sources like earthquakes, the signal classification seems to be characteristic for all of our avalanches and could be used for automatic detection.

5.1 Internal avalanche characteristics

We identified that class S2 is most likely related to the physical properties of the mass-movement inside the avalanche. We can use this to further analyse the internal structure of the avalanche propagating over the fiber-optic array. Since avalanche 3023 does not have a complex internal avalanche structure, but a well separated slow and fast part, we will look at a different avalanche. We chose avalanche 3016 for this analysis, since it is a single surge avalanche with a complex internal structure. From the clustering analysis, we know the frequency and apparent phase-velocity ranges of the mass-movement class S2. Hence, we focus on frequencies < 5 Hz and apparent phase velocities < 250 m/s (only downward propagating). The DAS data of a zoomed-in version of avalanche 3016 within this frequency and velocity range are displayed in Fig. 6.

Accordingly, we explain the low apparent phase velocities (< 6 m/s) with the avalanche's bulk mass motion, which may vary between avalanche events or even between surges of a single avalanche (Figure 2). Hence, in terms of avalanche processes, the classes S2 and S4 could be associated to different flow regimes within the avalanche - where the earlier class S2 may correspond to the high-energy processes occurring at the front of the avalanche, such as entrainment of snow or impacts of the (turbulent) suspensions with the ground, and class S4 may be related to the signal generated by the following dense basal layer and its deposition (Köhler, McElwaine, & Sovilla, 2018).

Another observation is, that the presence of some mass movement classes by themselves require additional analysis. A regional M 1.5 earthquake from Sanetschpass (see event 3036 in the supplementary material) is predominantly classified into classes S1 and S3. The classification of S1 and S3 during the regional earthquake also indicate that additional signals might be included in these classes. The absence of class S2 indicates that there is no mass movement present during the earthquake, but this non-uniqueness of the classification needs to be kept in mind for potential automatic classifications in the future.

6 Perspectives for Snow Avalanche Monitoring

DAS enables the distributed measurement of ground deformation in response to avalanche flow with high temporal and spatial resolution. There exist specific reasons why this could be a game changer for avalanche monitoring and warning applications. Our analysis shows that non-supervised classification of DAS recordings containing both noise and avalanche signatures is capable of separating the two. Although this method has to be applied to longer (multiple months) DAS records to evaluate its accuracy, the signal classes shared among all recorded avalanches suggests that automatic detections are feasible. The consistent detections of class S1 signals tens of seconds prior to the avalanche arrivals at the cable are particularly encouraging: interrogating pre-installed communication cables seems to be sensitive enough to detect avalanche seismograms remotely. This is important for the more realistic case where fiber-optic infrastructure locates parallel to pass roads or train lines, which are threatened by avalanche hazards in the lateral slopes and couloirs. For such cases snow avalanches will cross rather than propagate along fiber optic cables and longitudinal wave propagation as presented here will

be reduced. We can nevertheless expect to measure the seismic phases of classes S1, S2 and S3, which could be used to distinguish between powder snow avalanches containing a turbulent flow and pure dense snow avalanches (Köhler, Fischer, et al., 2018). How exactly such flow regime distinction manifests itself in the recognition of class S1, S2 and S3 signals remains to be seen. It may be necessary to further support classification with transition probabilities between states as has been done in previous application of machine learning algorithms to avalanche seismograms (Hammer et al., 2017; Heck et al., 2018). Finally, we stress the advantage of our Gaussian mixture models allowing for different states to coexist at the same time rather than identifying one single dominant state. Future classification could thus be improved with relative probabilities so that the "state mix" describes different parts and kinds of avalanches.

Our processing leverages signal coherence over a set of spatially distributed seismic sensors. Equivalent signal processing has already been used in the past for seismic signals of avalanches in the form of array methods (Lacroix & Helmstetter, 2011; Heck, Van Herwijnen, et al., 2019). In the present case, the unprecedented amount of seismic sensing locations was combined with unsupervised machine learning to automatically classify signals. To this, future applications could add waveform features (Chmiel et al., 2021) and image processing to further improve classification accuracy (Thrastarson et al., 2021). In any case, we do not expect user-defined threshold rules to perform better than our machine learning scheme since such methods cannot distinguish between signals with similar seismic amplitudes and frequency content.

Whereas this study focused on snow avalanches, the proposed DAS observation and signal classification could also be applied to other granular media like debris flows, rock-ice avalanches and smaller slope failures. Given seismogenesis of water turbulence (Gimbert et al., 2014), flood waves could be monitored and detected, as well. Our signals show that DAS is able to detect internal avalanche processes, which could be manifestations of roll-waves or shock waves. These internal waves are general features of open surface flows (Liu & Mei, 1994). Shock waves propagate as flow depth perturbations with larger waves traveling faster, which allows them to grow by "swallowing" smaller waves. The successive merging explains pulsing behavior of granular flows and frontal flow depths, which are much larger and thus more destructive than expected for steady flow (Zanuttigh & Lamberti, 2007; Razis et al., 2014; Viroulet et al., 2018). The detection of internal waves, which our DAS measurements provide, could therefore be a tool for better understanding and predicting maximum flow depths of granular flows and floods.

7 Challenges

Since the apparent phase velocity of an event propagating along the fiber is strongly dependent on the incidence angle of the event, it needs to be treated as a site- and event-specific property. Hence, the transferability of the trained Gaussian mixture model from the given test site to other installations might be limited. Nevertheless, the physical intuition we gained from the analyzed avalanches can be transferred to other sites and cable layouts.

A big challenge for monitoring hazardous alpine mass movements with DAS is the existence and access to fiber-optic infrastructure. Whereas the Vallée de la Sionne test site had accessible infrastructure existing for decades, sites like this are rare. The distribution of existing fibers in rural alpine areas, especially those that are subject to frequent hazardous mass movements, can be limited. In addition to fiber access, stable long-term power access for the interrogation unit can be challenging. If no fiber-optic infrastructure for data transfer exists, real-time monitoring and immediate early warning require a stable data transfer from the interrogation unit to the local responsible authorities. In case the fiber-optic infrastructure is required to be installed, the fiber needs to be protected against mass movement induced damages. For avalanche monitoring this means that the cable needs to be trenched deep enough and be protected against ero-

sion processes. We believe that the DAS technology can not only improve our understanding of hazardous mass movements from a scientific point of view by highlighting interactions between the mass movement and the subsurface, but can also improve seismic hazard monitoring and early warning solutions in the near-future.

8 Conclusions and Outlook

We have shown that the DAS technology is capable to measure avalanches propagating towards and on top of a fiber-optic cable. The avalanche signals measured from such a system include the seismo-acoustic near- and far-field as well as various mass movement regimes. By combining DAS with Bayesian Gaussian mixture models, we are able to extract key avalanche characteristics and their developments over both space and time. Significant importance for the classification are both the frequency content and the apparent phase velocities of the data within local time-space windows.

DAS adds new observations to the toolbox of mass movement research. With high-resolution recordings, DAS delivers data from the interface of the avalanche with the (sub)surface of the Earth. We observed indications of roll-waves. In the future, it can be envisioned that the Froude number could be calculated from the apparent velocities if the depth of the flow is known (similar to Pérez- Guillén et al. (2016)). Further research in amplitude calibration of DAS systems for mass movements is required, but a site-specific flow regime characterization based on DAS recordings and physical properties of strain rate measurements can be envisioned in the future.

The incorporation of subsurface strain (rate) as observed with DAS into numerical avalanche simulation tools could increase the usability of DAS data in the field of avalanche dynamics research even further.

Acknowledgments

The authors want to thank everyone involved in the field campaign and the discussion of the results. Especially, we want to thank Emma Suriñach for constructive discussions about seismic measurements of avalanches. Our colleagues at WSL, SLF and ETH Zürich for feedback on the data processing and the applied methods, and Athena Chalari and the Silixa support team for their technical assistance of our iDAS(TM) interrogation unit. PP also wants to acknowledge the IRIS DAS research coordination network, especially discussions within their Machine Learning working group.

Data availability statement

The data of the two avalanche examples will be made available upon publication on Zenodo in the Snow Avalanche Dynamics Community. Since the Bayesian Gaussian Mixture model depends on a wide range of tuning parameters, the trained model will be made available. The extracted features for both avalanche examples will also be made available upon publication.

Appendix A Schematic Avalanche Propagating Over DAS Array

Appendix B Background Information on Avalanches Discussed in this Manuscript

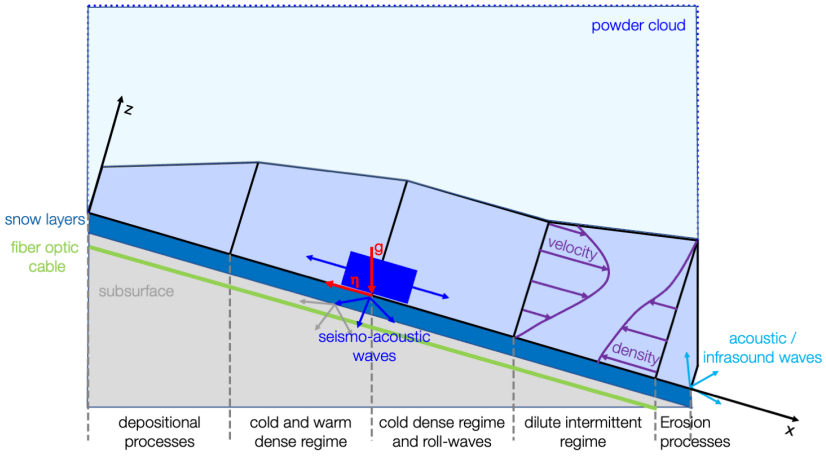

Figure A1. Schematic avalanche processes generating seismo-acoustic signals. The velocity and density profile vary with depth (z). The propagation of the avalanche downhill (x) results in acoustic infrasound waves in the air, as well as seismo-acoustic waves due to sliding friction, depositional mechanisms, and interaction of the mass movement with the topography. In this experiment, the fiber-optic cable is located in a conduit in the subsurface, over which the avalanches propagate. Figure schematically after Pérez- Guillén et al. (2016) and Sovilla et al. (2015).

Table B1. Avalanche characteristics of the events discussed in this manuscript. The duration indicates the time the avalanches are propagating on top of the fiber-optic array.

Number	Date of occurrence	Duration	Characteristics
Avalanche 3005	2021-01-02	? minutes	- Very small avalanche - Did not reach the cable - No surges visible
Avalanche 3009	2021-01-15	4 minutes	- Large transitional powder snow avalanche - Fast and dilute component - 3 main surges - Depositional tail
Avalanche 3016	2021-01-25	1 minute	- Powder snow avalanche - No dense transition - Depositional tail
Avalanche 3020	2021-01-27	0.5 minutes	- Small powder snow avalanche - No dense transition - One surge
Avalanche 3021	2021-01-28	1 minute	- Dense avalanche - Depositional tail - One big surge
Avalanche 3022	2021-01-28	2.5 minutes	- Large transitional powder snow avalanche - Depositional tail
Avalanche 3023	2021-01-28	3 minutes	- Large powder snow avalanche - Partial transition - Fast and slow part - Well separated - Long tail
Avalanche 3024	2021-01-28	? minutes	- Large transitional powder snow avalanche - Not over array
Avalanche 3026	2021-01-31	? minutes	- No avalanche visible
Avalanche 3027	2021-02-01	? minutes	- Small one-surge powder snow avalanche - Not over array
Avalanche 3028	2021-02-01	? minutes	- Large multi-surge snow avalanche - Not over array - Too far away
Avalanche 3030	2021-02-08	? minutes	- No avalanche visible
Event 3036	2021-03-03	< 0.3 minutes	- Regional earthquake M1.2 at Sanetschpass - No avalanche

Appendix C Additional plots

Additional plots of the avalanche candidates in Tab. B1 with their corresponding predicted classes from the clustering algorithm can be found in the supplementary material.

References

Allstadt, K. E., Matoza, R. S., Lockhart, A. B., Moran, S. C., Caplan-Auerbach, J., Haney, M. M., ... Malone, S. D. (2018). Seismic and acoustic signatures of surficial mass movements at volcanoes. *Journal of Volcanology and Geothermal Research*, *364*, 76-106. Retrieved from `https://www.sciencedirect.com/science/article/pii/S0377027317306261` doi: https://doi.org/10.1016/j.jvolgeores.2018.09.007

Alpaydin, E. (2020). *Introduction to machine learning*. MIT press.

Ammann, W. J. (1999). A new swiss test-site for avalanche experiments in the vallée de la sionne/valais. *Cold Regions Science and Technology*, *30*(1-3), 3–11.

Arattano, M., & Marchi, L. (2008). Systems and sensors for debris-flow monitoring and warning. *Sensors*, *8*(4), 2436–2452.

Bishop, C. M., & Nasrabadi, N. M. (2006). *Pattern recognition and machine learning* (Vol. 4) (No. 4). Springer.

Boore, D. M., & Joyner, W. B. (1997). Site amplifications for generic rock sites. *Bulletin of the seismological society of America*, *87*(2), 327–341.

Capelli, A., Kapil, J. C., Reiweger, I., Or, D., & Schweizer, J. (2016). Speed and attenuation of acoustic waves in snow: Laboratory experiments and modeling with biot's theory. *Cold Regions Science and Technology*, *125*, 1–11.

Carroll, C., Turnbull, B., & Louge, M. (2012). Role of fluid density in shaping eruption currents driven by frontal particle blow-out. *Physics of Fluids*, *24*(6), 066603.

Chmiel, M., Walter, F., Wenner, M., Zhang, Z., McArdell, B. W., & Hibert, C. (2021). Machine learning improves debris flow warning. *Geophysical Research Letters*, *48*(3), e2020GL090874. Retrieved from `https://agupubs.onlinelibrary.wiley.com/doi/abs/10.1029/2020GL090874` (e2020GL090874 2020GL090874) doi: https://doi.org/10.1029/2020GL090874

Dilley, M. (2005). *Natural disaster hotspots: a global risk analysis* (Vol. 5). World Bank Publications.

Edwards, A., & Gray, J. (2015). Erosion–deposition waves in shallow granular free-surface flows. *Journal of Fluid Mechanics*, *762*, 35–67.

Emberson, R., Kirschbaum, D., & Stanley, T. (2020). New global characterisation of landslide exposure. *Natural Hazards and Earth System Sciences*, *20*(12), 3413–3424.

Froude, M. J., & Petley, D. N. (2018). Global fatal landslide occurrence from 2004 to 2016. *Natural Hazards and Earth System Sciences*, *18*(8), 2161–2181.

Gimbert, F., Tsai, V. C., & Lamb, M. P. (2014). A physical model for seismic noise generation by turbulent flow in rivers. *Journal of Geophysical Research: Earth Surface*, *119*(10), 2209–2238.

Grimm, J. (2021). Cryoseismic event analysis on distributed strain recordings leveraging statistical learning methods. *MSc. Thesis, ETH Zürich*.

Grimm, J., & Poli, P. (2022). *Making sense of urban das data with clustering of coherence-based array features* (Tech. Rep.). EGU2022: Copernicus Meetings.

Hammer, C., Fäh, D., & Ohrnberger, M. (2017). Automatic detection of wet-snow avalanche seismic signals. *Natural hazards*, *86*(2), 601–618.

Hartog, A. H. (2017). *An introduction to distributed optical fibre sensors*. CRC press.

Heck, M., Hammer, C., van Herwijnen, A., Schweizer, J., & Fäh, D. (2018). Au-

tomatic detection of snow avalanches in continuous seismic data using hidden markov models. *Natural Hazards and Earth System Sciences*, *18*(1), 383–396.

Heck, M., Hobiger, M., Van Herwijnen, A., Schweizer, J., & Fäh, D. (2019). Localization of seismic events produced by avalanches using multiple signal classification. *Geophysical Journal International*, *216*(1), 201–217.

Heck, M., Van Herwijnen, A., Hammer, C., Hobiger, M., Schweizer, J., & Fäh, D. (2019). Automatic detection of avalanches combining array classification and localization. *Earth Surface Dynamics*, *7*(2), 491–503.

Iten, M., Puzrin, A. M., & Schmid, A. (2008). Landslide monitoring using a road-embedded optical fiber sensor. In W. Ecke, K. J. Peters, & N. G. Meyendorf (Eds.), *Smart sensor phenomena, technology, networks, and systems 2008* (Vol. 6933, pp. 328 – 336). SPIE. Retrieved from `https://doi.org/10.1117/12.774515` doi: 10.1117/12.774515

Keylock, C., Ash, M., Vriend, N., Brennan, P., McEwaine, J., & Sovilla, B. (2014). Looking inside an avalanche using a novel radar system. *Geology Today*, *30*(1), 21–25.

Klaasen, S., Paitz, P., Lindner, N., Dettmer, J., & Fichtner, A. (2021). Distributed acoustic sensing in volcano-glacial environments—mount meager, british columbia. *Journal of Geophysical Research: Solid Earth*, *126*(11), e2021JB022358. Retrieved from `https://agupubs.onlinelibrary.wiley.com/doi/abs/10.1029/2021JB022358` (e2021JB022358 2021JB022358) doi: https://doi.org/10.1029/2021JB022358

Köhler, A., Fischer, J.-T., Scandroglio, R., Bavay, M., McElwaine, J., & Sovilla, B. (2018). Cold-to-warm flow regime transition in snow avalanches. *The Cryosphere*, *12*(12), 3759–3774.

Köhler, A., McElwaine, J., & Sovilla, B. (2018). Geodar data and the flow regimes of snow avalanches. *Journal of geophysical research: earth surface*, *123*(6), 1272–1294.

Lacroix, P., & Helmstetter, A. (2011). Location of seismic signals associated with microearthquakes and rockfalls on the séchilienne landslide, french alps. *Bulletin of the Seismological Society of America*, *101*(1), 341–353.

Leinss, S., Wicki, R., Holenstein, S., Baffelli, S., & Bühler, Y. (2020). Snow avalanche detection and mapping in multitemporal and multiorbital radar images from terrasar-x and sentinel-1. *Natural Hazards and Earth System Sciences*, *20*(6), 1783–1803.

Lindsey, N. J., Dawe, T. C., & Ajo-Franklin, J. B. (2019). Illuminating seafloor faults and ocean dynamics with dark fiber distributed acoustic sensing. *Science*, *366*(6469), 1103–1107.

Lindsey, N. J., & Martin, E. R. (2021). Fiber-optic seismology. *Annual Review of Earth and Planetary Sciences*, *49*, 309–336.

Lindsey, N. J., Rademacher, H., & Ajo-Franklin, J. B. (2020). On the broadband instrument response of fiber-optic das arrays. *Journal of Geophysical Research: Solid Earth*, *125*(2), e2019JB018145.

Liu, K.-f., & Mei, C. C. (1994). Roll waves on a layer of a muddy fluid flowing down a gentle slope—a bingham model. *Physics of Fluids*, *6*(8), 2577–2590.

Marchetti, E., Walter, F., Barfucci, G., Genco, R., Wenner, M., Ripepe, M., ... Price, C. (2019). Infrasound array analysis of debris flow activity and implication for early warning. *Journal of Geophysical Research: Earth Surface*, *124*(2), 567-587. Retrieved from `https://agupubs.onlinelibrary.wiley.com/doi/abs/10.1029/2018JF004785` doi: https://doi.org/10.1029/2018JF004785

Marchetti, E., Walter, F., & Meier, L. (2021). Broadband infrasound signal of a collapsing hanging glacier. *Geophysical Research Letters*, *48*(16), e2021GL093579.

Martin, E. R., Huot, F., Ma, Y., Cieplicki, R., Cole, S., Karrenbach, M., & Biondi,

B. L. (2018). A seismic shift in scalable acquisition demands new processing: Fiber-optic seismic signal retrieval in urban areas with unsupervised learning for coherent noise removal. *IEEE Signal Processing Magazine*, *35*(2), 31–40.

Michlmayr, G., Chalari, A., Clarke, A., & Or, D. (2017). Fiber-optic high-resolution acoustic emission (ae) monitoring of slope failure. *Landslides*, *14*(3), 1139–1146.

Minardo, A., Catalano, E., Coscetta, A., Zeni, G., Zhang, L., Di Maio, C., ... Zeni, L. (2018). Distributed fiber optic sensors for the monitoring of a tunnel crossing a landslide. *Remote Sensing*, *10*(8). Retrieved from `https://www.mdpi.com/2072-4292/10/8/1291` doi: 10.3390/rs10081291

Paitz, P., Edme, P., Gräff, D., Walter, F., Doetsch, J., Chalari, A., ... Fichtner, A. (2021). Empirical investigations of the instrument response for distributed acoustic sensing (das) across 17 octaves. *Bulletin of the Seismological Society of America*, *111*(1), 1–10.

Pedregosa, F., Varoquaux, G., Gramfort, A., Michel, V., Thirion, B., Grisel, O., ... Duchesnay, E. (2011). Scikit-learn: Machine learning in Python. *Journal of Machine Learning Research*, *12*, 2825–2830.

Petley, D. (2012). Global patterns of loss of life from landslides. *Geology*, *40*(10), 927–930.

Press, W. H., Teukolsky, S. A., Vetterling, W. T., & Flannery, B. P. (2007). *Numerical recipes 3rd edition: The art of scientific computing*. Cambridge university press.

Prokop, A., Schön, P., Wirbel, A., & Jungmayr, M. (2014). Monitoring avalanche activity using distributed acoustic fiber optic sensing. In *Proceedings of the international snow science workshop* (pp. 129–133).

Pérez- Guillén, C., Sovilla, B., Suriñach, E., Tapia, M., & Köhler, A. (2016). Deducing avalanche size and flow regimes from seismic measurements. *Cold Regions Science and Technology*, *121*, 25-41. Retrieved from `https://www.sciencedirect.com/science/article/pii/S0165232X15002177` doi: https://doi.org/10.1016/j.coldregions.2015.10.004

Razis, D., Edwards, A., Gray, J., & van der Weele, K. (2014). Arrested coarsening of granular roll waves. *Physics of Fluids*, *26*(12), 123305.

Sánchez-Sesma, F. J., Weaver, R. L., Kawase, H., Matsushima, S., Luzón, F., & Campillo, M. (2011). Energy partitions among elastic waves for dynamic surface loads in a semi-infinite solid. *Bulletin of the Seismological Society of America*, *101*(4), 1704–1709.

Scott, D. W. (2015). *Multivariate density estimation: theory, practice, and visualization*. John Wiley & Sons.

Sovilla, B., Burlando, P., & Bartelt, P. (2006). Field experiments and numerical modeling of mass entrainment in snow avalanches. *Journal of Geophysical Research: Earth Surface*, *111*(F3).

Sovilla, B., McElwaine, J. N., & Louge, M. Y. (2015). The structure of powder snow avalanches. *Comptes Rendus Physique*, *16*(1), 97-104. Retrieved from `https://www.sciencedirect.com/science/article/pii/S1631070514001844` (Granular physics / Physique des milieux granulaires) doi: https://doi.org/10.1016/j.crhy.2014.11.005

Steinkogler, W., Gaume, J., Löwe, H., Sovilla, B., & Lehning, M. (2015). Granulation of snow: From tumbler experiments to discrete element simulations. *Journal of Geophysical Research: Earth Surface*, *120*(6), 1107–1126.

SwissTopo. (2021). *Online tool for Swiss Raster images*. `https://www.swisstopo.admin.ch/de/geodata/maps/smr/smr10.html`. ([Online; accessed 24-February-2022])

Thrastarson, S., Torfason, R., Klaasen, S., Paitz, P., CUBUK SABUNCU, Y., Jónsdóttir, K., & Fichtner, A. (2021). Detecting seismic events with computer vision: Applications for fiber-optic sensing. *Earth and Space Science Open*

Archive, 19. Retrieved from https://doi.org/10.1002/essoar.10509693.1 doi: 10.1002/essoar.10509693.1

Tregaskis, C., Johnson, C., Cui, X., & Gray, J. (2022). Subcritical and supercritical granular flow around an obstacle on a rough inclined plane. *Journal of Fluid Mechanics*, *933*.

Tsai, V. C., Minchew, B., Lamb, M. P., & Ampuero, J.-P. (2012). A physical model for seismic noise generation from sediment transport in rivers. *Geophysical Research Letters*, *39*(2).

Van Herwijnen, A., & Schweizer, J. (2011). Monitoring avalanche activity using a seismic sensor. *Cold Regions Science and Technology*, *69*(2-3), 165–176.

Viroulet, S., Baker, J. L., Rocha, F. M., Johnson, C. G., Kokelaar, B. P., & Gray, J. M. N. T. (2018). The kinematics of bidisperse granular roll waves. *Journal of Fluid Mechanics*, *848*, 836–875. doi: 10.1017/jfm.2018.348

Walter, F., Gräff, D., Lindner, F., Paitz, P., Köpfli, M., Chmiel, M., & Fichtner, A. (2020). Distributed acoustic sensing of microseismic sources and wave propagation in glaciated terrain. *Nature communications*, *11*(1), 1–10.

Wenner, M., Allstadt, K., Thelen, W., Lockhart, A., Hirschberg, J., McArdell, B. W., & Walter, F. (2022). Seismometer records of ground tilt induced by debris flows. *Bulletin of the Seismological Society of America*, *112*(5), 2376–2395.

Williams, E. F., Fernández-Ruiz, M. R., Magalhaes, R., Vanthillo, R., Zhan, Z., González-Herráez, M., & Martins, H. F. (2019). Distributed sensing of microseisms and teleseisms with submarine dark fibers. *Nature communications*, *10*(1), 1–11.

Yu, Z., Dai, H., Zhang, Q., Zhang, M., Liu, L., Zhang, J., & Jin, X. (2018). High-resolution distributed strain sensing system for landslide monitoring. *Optik*, *158*, 91-96. Retrieved from https://www.sciencedirect.com/science/article/pii/S0030402617316418 doi: https://doi.org/10.1016/j.ijleo.2017.12.013

Zanuttigh, B., & Lamberti, A. (2007). Instability and surge development in debris flows. *Reviews of Geophysics*, *45*(3).

Zhan, Z. (2019). Distributed Acoustic Sensing Turns Fiber-Optic Cables into Sensitive Seismic Antennas. *Seismological Research Letters*, *91*(1), 1-15. Retrieved from https://doi.org/10.1785/0220190112 doi: 10.1785/0220190112

Zhongming, Z., Linong, L., Xiaona, Y., Wangqiang, Z., & Wei, L. e. a. (2021). Ar6 climate change 2021: The physical science basis. *2021 IPCC report*.